Article

Adsorption of Methylene Blue Dye and Analysis of Two Clays: A Study of Kinetics, Thermodynamics, and Modeling with DFT, MD, and MC Simulations

Sarra Sellak, Jaouad Bensalah,* Hanae Ouaddari, Zaki Safi, Avni Berisha, Khalid Draoui, Ilias Barrak, Taoufiq Guedira, Mohammed Bourhia, Samir Ibenmoussa, Mohammad Okla, Musaab Dauelbait,* Amar Habsaoui, and Mohamed Harcharras

Read Online

ACCESS | Metrics & More | Article Recommendations

ABSTRACT: The purpose of this research was to learn more about the primary and secondary properties of Moroccan natural clay in an effort to better investigate innovative adsorbents and gain access to an ideal adsorption system. Scanning electron microscopy coupled with energy-dispersive X-ray spectroscopy analysis (SEM-EDX) and X-ray fluorescence were employed for identification. SEM revealed clay grains, including tiny particles and unevenly shaped sticks. First- and second-order rate laws, representing two distinct kinetic models, were applied in the kinetic approach. Adsorption of dye MB onto natural clay was studied, and the results agreed with the 2 s order model. The significant correlation coefficients support the inference that the adsorption process was governed by the Langmuir model. Subsequent DFT analyses demonstrated that the methylene blue dye's HOMO and LUMO surfaces are dispersed across most of the dye's components, pointing to a strong interaction with the clay. To determine how the dye might be adsorbed onto the clay, we employed quantum descriptors to locate its most nucleophilic and electrophilic centers. Endothermic reactions are evident during the MB adsorption process on clay, as indicated by the positive values of ΔH^0 and ΔS^0 (70.49 kJ mol^{-1} of RC and 84.19 kJ mol^{-1} of OC and 10.45 J mol^{-1} K^{-1} of RC and 12.68 mol^{-1} K^{-1} of OC, respectively). Additionally dye molecules on the adsorbent exhibit a higher order of distribution than in the solution, indicating that the adsorption process is spontaneous.
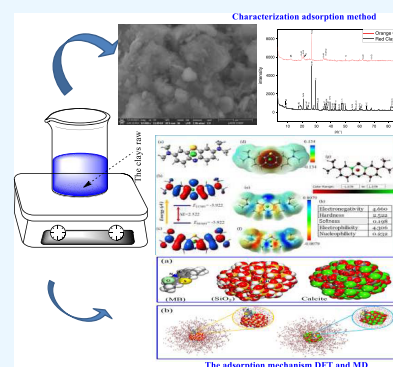
1. INTRODUCTION

Today, wastewater resources face severe depletion as a result of demographic growth and heavy industrialization, leading to the discharge of untreated wastewater into the environment. Industrial effluents, especially those from the textile industry, contain large quantities of dyes that are not only toxic but also potentially carcinogenic, posing significant hazards to human health.[1,2] Hence there is the need to develop processes that protect water resources from pollution by treating polluted water at the source. Therefore, these industrial effluents must be treated to lessen their negative effects on the natural world. Because in light of the gravity of this environmental issue, a lot of effort has been put into water pollution control, and a number of pollution control processes have been developed.[3,4] Electro-dialysis, phothocatalysis, ion exchange, chemical precipitation, nanofiltration, and ion exchange resins are all examples of methods,[5,6] such as coagulation,[7] adsorption, etc. However, adsorption remains one of the most widely adopted techniques due to its insensitivity to toxic substances and its low application cost.[8] For less expensive pollution control, easily accessible and practical adsorbents like clays are of great interest.[9,10] Several

research studies have reported the efficacy of clays in adsorbing contaminants.[9,11,12] The aim of this research is to examine the adsorption capacity of two natural clays sampled in the Rabat region, specifically focusing on the adsorption of methylene blue (MB). In order to learn more about adsorbents, we utilized XRF, FTIR, XRD, and SEM. Adsorption of MB by OC and RC was further investigated by predicting it using kinetic and isothermal data obtained from experiments. Parameters were determined by employing both kinetic and isothermal models, and the results were compared. To identify the most accurate model variants, R^2 coefficients of determination were computed.

The characterization of the adsorbent by FTIR and XRD following MB adsorption, as well as adsorption isotherms, was

Figure 1. Rough-hewn depictions of clay Rabat-Sale-Morocco operational to date.

employed to assess the investigation of the adsorption mechanism.

2. MATERIALS AND METHODS

2.1. Preparation of Adsorbents. The clay samples were collected in Rabat-Sale-Morocco (Figure 1). Next, samples were washed several times with demineralized water before being exploited in the experiments. The solid sample was dried at 105 °C for 24 h, crushed, and sieved through a 140 μm sieve.

2.2. Preparation of the Solution. Methylene blue was purchased from Solvachim (Morocco). The structure of the MB molecule, which is a cationic dye, of chemical formula $C_{16}H_{18}N_3SCl$ and molar mass of 319.85 mol·g^{-1} is given in Figure 2.
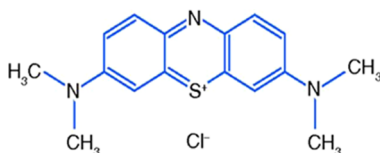

Figure 2. Structure of methylene blue.

2.3. Experimental Section. *2.3.1. Characterization of Clays.* Physical characterization methods like Fourier transform infrared spectroscopy (FTIR) were employed to learn more about the clays before and after their utilization in the experiments. The FTIR was conducted using Bruker vector 70 spectrometer, and the measurements were taken between 400 and 4000 cm^{-1} at a resolution of 2 cm^{-1}. In terms of their chemical makeup, X-ray fluorescence spectroscopy was used to differentiate between the two materials, and it was an "Axion" model used, with a wavelength dispersion of 1 kW. X-ray diffractometry was used to analyze the clays for the structural characteristics. Scanning electron microscopy (SEM) was used to examine the morphologies of both the OC and RC samples. The HIROX SH-4000 M coupled with energy-dispersive X-ray spectroscopy (EDX) was employed for this analysis.[6,8,11]

2.3.2. PH(PZC) at the Zero Charge Point. The zero charge point (PZC) was found by using a sodium chloride solution. The PZC is defined as the pH value at which there is no net charge on the entire surface The PZC is defined as the pH value

at which there is no net charge on the entire surface. In 9 separate beakers, each containing 20 mL of a 0.1 M sodium chloride solution, both HCl and NaOH (0.1 M) were employed to adjust the initial pH from 2 to 12. In each beaker, 0.1 g of OC and RC was added, and the mixtures were stirred using a magnetic stirrer at room temperature for 24 h. Subsequently, the supernatant was tested for the pH after centrifugation. The zero charge point (PZC) was determined as the intersection of the pH variation curve with the initial pH.[13]

2.4. Adsorption Studies. *2.4.1. Adsorption Kinetics.* Experiments on adsorption were conducted at pH = 6 and constant temperatures of T = 20, 40, and 60 °C. The adsorption duration was set at 3 h with 600 rpm agitation. A methylene blue solution (25 mL of initial concentration Ci varying between 20 and 500 mg·L^{-1}) was in contact with a mass of 0.04 g of the adsorbents. After the reaction is complete, the mixtures underwent UV/V analysis after being filtered. UV/visible filtering and analysis: A UV/visible spectrophotometer calibration curve was used to calculate residual concentration Ce (Shimadzu, UV-1240) at $\lambda 1/4$ 664 nm. The adsorbed amount is calculated using the following formula

$$Q_{ads} = (C_0 - C_e) \times \frac{m}{V} \tag{1}$$

Q_{ads}: adsorption capacity (mg·g^{-1}), C_0: initial MB concentration (mg·L^{-1}), C_e: residual concentration of MB (mg·L^{-1}), m_{ads}: adsorbent mass used (g), and V_{sol}: volume of the MB solution (L).

2.4.2. Kinetic and Isothermal Modeling. To comprehend the adsorption mechanism of the MB on the two clays (OC and RC), adsorption kinetics modeling was performed using the pseudo-first-order, pseudo-second-order, and intraparticle Weber–Morris models:

Pseudo-first-order

$$\log (q_e - q_t) = \log (q_e) - \left(\frac{k_1}{2.203} \right) \times t \tag{2}$$

Pseudo-second-order

$$\frac{t}{q_t} = \frac{1}{K_2 \times q_e^2} + \frac{1}{q_e} \times t \tag{3}$$

Table 1. Data Are from Chemical and Mineralogical Analysis of RC and OC

clay	SiO_2	Al_2O_3	Fe_2O_3	MgO	CaO	Na_2O	K_2O	LOI
orange clay (OC)	53.01	23.59	8.299	1.691	0.4340	0.7626	2.610	7.980
red clay (RC)	47.15	25.44	17.13	0.973	0.3214	0.3053	1.753	17.13

Figure 3. X-ray diffraction spectra of the OC and RC.

Figure 4. Infrared spectra of OC and RC before and after adsorption.

$$q_t = K_3 \times t^{0.5} + c \tag{4}$$

Langmuir and Freundlich models were used for isotherms
Langmuir

$$Q_e = \frac{q_m \times K_L \times C_e}{1 + K_L \times C_e} \tag{5}$$

K_L: Langmuir constant and q_m: maximum amount of solute adsorption to solid phase in $(mg \cdot g^{-1})$. The two constants K_L and q_m can be calculated from the following linear form

$$\frac{C_e}{Q_e} = \frac{1}{K_L \times q_m} + \frac{C_e}{q_m} \tag{6}$$

3D top-lighted rightwards arrowhead symbol Fruendlich

$$Q_e = K_F \times C_e^{1/n} \tag{7}$$

Q_e: amount of adsorption in $mg \cdot g^{-1}$, K_F: Freundlich constant that expresses adsorption affinity $(L \cdot mg^{-1})$, C_e: equilibrium concentration of solute in $mg \cdot L^{-1}$, and $1/n$: Freundlich constant that translates the adsorption intensity.

The constants K_F and $1/n$ can be determined in the following linear form

$$\log(q_e) = \log(K_F) + \frac{1}{n} \times \log(C_e) \tag{8}$$

Error analysis calculations, including the coefficient of determination, proved the accuracy of these models (R^2).
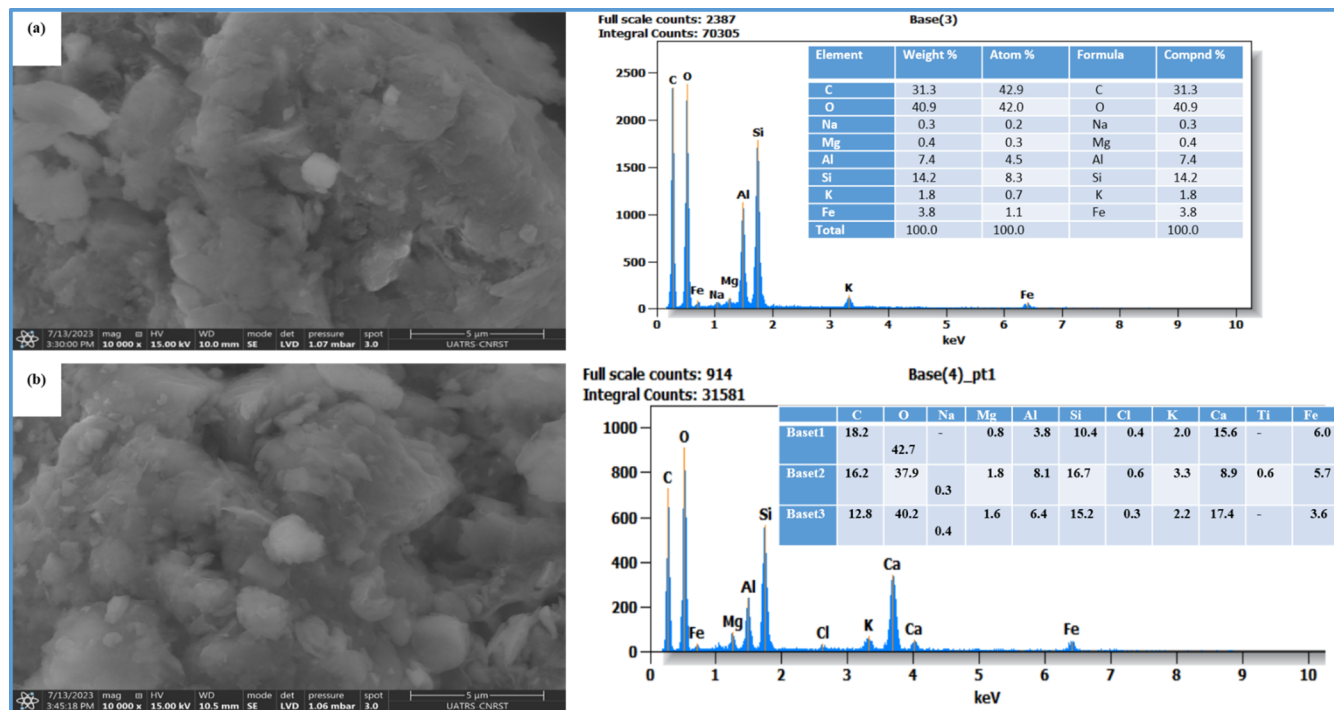
Figure 5. SEM images and respective EDX spectra of the clay's OC (a) and RC (b).

3. RESULTS AND DISCUSSION

3.1. Characterization. *3.1.1. X-ray Fluorescence Analysis.* According to the data of the chemical and mineralogical analysis of clays RC and OC presented in Table 1, silicon oxide is the major constituent for both clays, justified by the presence of free silica. The highest amount was detected for orange clay (53%). Aluminum oxide is present with a significant amount in both clays (>13%). Additionally, red clay exhibits highest amount of iron oxide (17.13%).

These results can help in determining the suitable applications of these materials. Clays are rich in iron and Al and Ca might be good candidates for the adsorption of anions due to their affinity toward these elements.[14] The fire loss or LOI shown in Table 1 corresponds to the mass loss resulting from heat treatment of a sample. Determination of this quantity allows us to estimate the rate of the organic matter and carbonates present in a sample. It is observed that the highest value of fire loss was measured for red clay.[15,16] This outcome suggests a lower presence of organic matter compared to that of the mineral fraction, explaining the total absence of characteristic bands of organic matter in the infrared analyses for both solids.

3.1.2. X-ray Diffraction. Figure 3 represents the powder diffractograms X of the two clays, indicating that the clay fraction of the orange clay consists mainly of muscovite and a low content of dolomite with the significant presence of calcite. On the other hand, red clay appears to be a mixture of kaolinite and muscovite. Additionally, both clays exhibit the noteworthy presence of quartz as associated minerals.

3.1.3. FTIR Spectroscopy. In order to better define the natural clay minerals, the FTIR spectra are combined in Figure 4 to provide a comprehensive analysis.

Both clays' infrared spectra are displayed in Figure 4. Generally, the adsorption bands that appear in the 3700−3620 cm^{-1} region correspond to the vibrations of the characteristic structural hydroxyl groups of kaolinite.[17] The type of bonds in the molecules determines the location and strength of these bands. In red clay, these bands appear around 3620.99 cm^{-1}, while in orange clay, they are observed around 3617.5 cm^{-1}. The bands at approximately 3380 and 1631.92 cm^{-1} for orange clay correspond to the elongation and deformation vibrations of the adsorbed water OH group.[17,18] While the characteristic bands of carbonates were detected in orange clay around 1416.67 cm^{-1}, quartz displays the signature deformation vibrational bands associated with the Si−O bond for red clay around 460.11 and 513.69 cm^{-1}, and the bands at 981.98 and 987.67 cm^{-1} are attributed to Al−OH−Al deformation.[19]

The FTIR spectra of OG and RC before and after MB adsorption are shown in Figure 5. A decrease is observed in the intensity of the internal OH group bands of the structure, which are located at 3696.99 and 3314.16 cm^{-1}, followed by an evolution and shift of the valence vibrational bands located around 1638.98 cm^{-1}, which can be attributed to aromatic CH−N and which overlap with the vibrational bands of the adsorbed OH group.

New peaks appear in the spectra, evolving remarkably locally for orange clay at around 1398.8 cm^{-1}, confirming the presence of the aromatic C═C group, while bands at around 1353.28 and 1336.82 cm^{-1}, indicate the presence of aliphatic CH, and for the red clay, around 1200 cm^{-1} could be attributed to the valence vibration of −C−N and N−N (stretching). It is observed that the shift in wavenumber corresponds to the variation in the energy of the functional groups, indicating the existence of an MB binding process on the clay surface.

3.1.4. SEM/EDX. The elemental chemical composition of the clay was subjectively estimated with the use of an analytical microscope (SEM) and an energy-dispersive X-ray spectrometer (EDX) (Figure 5).

The included EDX spectra and micrographs of OC and RC depict an assembly like arrangement of sample particles, including aggregates and small grains. Additionally, these images reveal larger holes in the OC sample compared to the RC sample.[11,14,19,20]
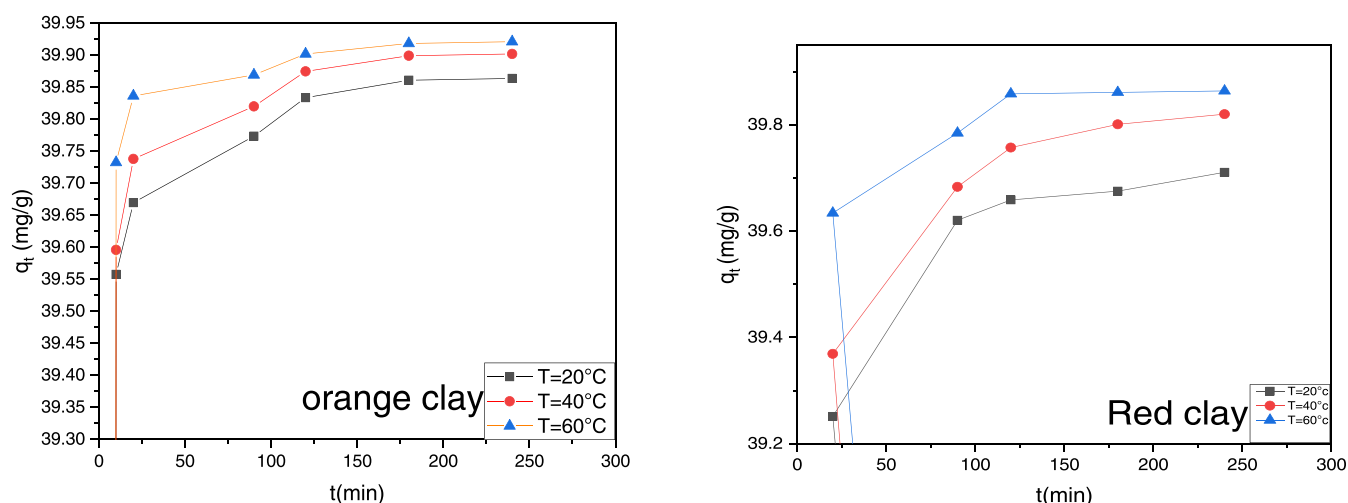
Figure 6. MB adsorption kinetics ($C_0 = 80$ mg·L^{-1}) on the OC and RC at pH = 6.0.

Table 2. Kinetic Parameters of MB Adsorption modeling at Different Temperatures on OC and RC

	clay		orange clay			red clay	
models	Qe-$_{exp}$ (mg·g^{-1})	39.87	39.91	39.93	39.76	39.81	39.87
	T (°C)	20	40	60	20	40	60
LPFO	q_e (mg·g^{-1})	0.330	0.290	0.160	0.920	1.926	0.88
	k_1 (min^{-1})	0.017	0.016	0.012	0.003	0.006	0.002
	R_1^2	0.966	0.959	0.944	0.927	0.926	0.741
LPSO	q_e (mg·g^{-1})	39.88	39.92	39.93	39.76	39.87	39.9
	K_2 (g·mg^{-1}·min^{-1})	0.190	0.208	0.340	0.075	0.067	0.104
	R_1^2	1	1	1	1	1	1

Al, Si, and O can be seen as the most abundant elements in both clays in the EDX spectra. These findings corroborate the XRD findings that the primary component of red clay is kaolinite, muscovite, and quartz. On the other hand, we note the dominance of carbon in orange clay due to the significant presence of calcite.[19−25]

3.2. Adsorption Studies. *3.2.1. Adsorption Kinetics.* The adsorption kinetics of MB on OC and RC at different temperatures are illustrated in Figure 6 below. For contact times less than 4 h at all temperatures, significant amounts of adsorbate are adsorbed for OC with values at T = 20, 40, and 60 °C being 39.86, 39.39, and 39.92 mg·g^{-1} and for CR being 39.76, 39.81, and 39.87 mg·g^{-1}, respectively. Adsorbed mass rises as temperature rises, which can be attributed to higher temperatures breaking down the covalent connections between the dye molecules and the active sites of the adsorbents.

It is likely that as temperatures increase, the MB diffuses more rapidly via the clay minerals' interior pores. Conversely, this structural alteration may cause inflation in OC and RC, potentially impacting the penetration of larger methylene blue molecules.

The adsorption mechanism of MB on the two adsorbents must be determined, and the experimental points were analyzed using the pseudo-first-order kinetic model and the pseudo-second-order model. To identify the most suitable model, experimental data were analyzed using R^2 calculations (Table 2). The kinetic parameters can be found by solving the aforementioned linear systems of equations. The values generated from the various kinetic parameters are shown in Table 2, and the curves of the pseudo-first-order and pseudo-second-order models are shown in Figure 7. In light of these considerations, we find that the experimental data for all three

adsorption temperatures are well described by the pseudo-second-order model. Table 2 shows that the calculated values of q$_{cal}$ are in close agreement with the experimental values of q_{exp}. Additionally, the values for the pseudo-second-order model's velocity constants k_2 rise from 20 to 60 °C. Coefficient of determination values also supported this finding, R^2 very close to 1.

The diffusion process of the solution's MB to the external and internal surface of the OC and RC was studied by plotting q_t as a function of t$^{0.5}$, which was used to test the Weber−Morris intraparticle model. Using this model for the two adsorbents, shown graphically in Figure 8, reveals that MB adsorption proceeds via two distinct phases for each solid. The first step is surface adsorption, and the second step is intraparticle diffusion. The kinetic parameters of the diffusion model for the adsorption of MB by red clay and orange clay are shown in Table 3. The diffusion coefficients of the two adsorbents decrease with time but do not vary with the temperatures. The diffusion constants for MB by red clay are higher than those for orange clay during the initial diffusion phase across the three temperatures. However, for the second adsorption step, the diffusion constants of the two dyes are very close. This indicates that the adsorption of MB by red clay is faster than the adsorption of MB by orange clay during the initial phase of the process.

The activation energies can be calculated from the pseudo-second-order rate constant (k_2) using the Arrhenius equation

$$\ln K_2 = \ln (A) - \frac{E_a}{RT}$$

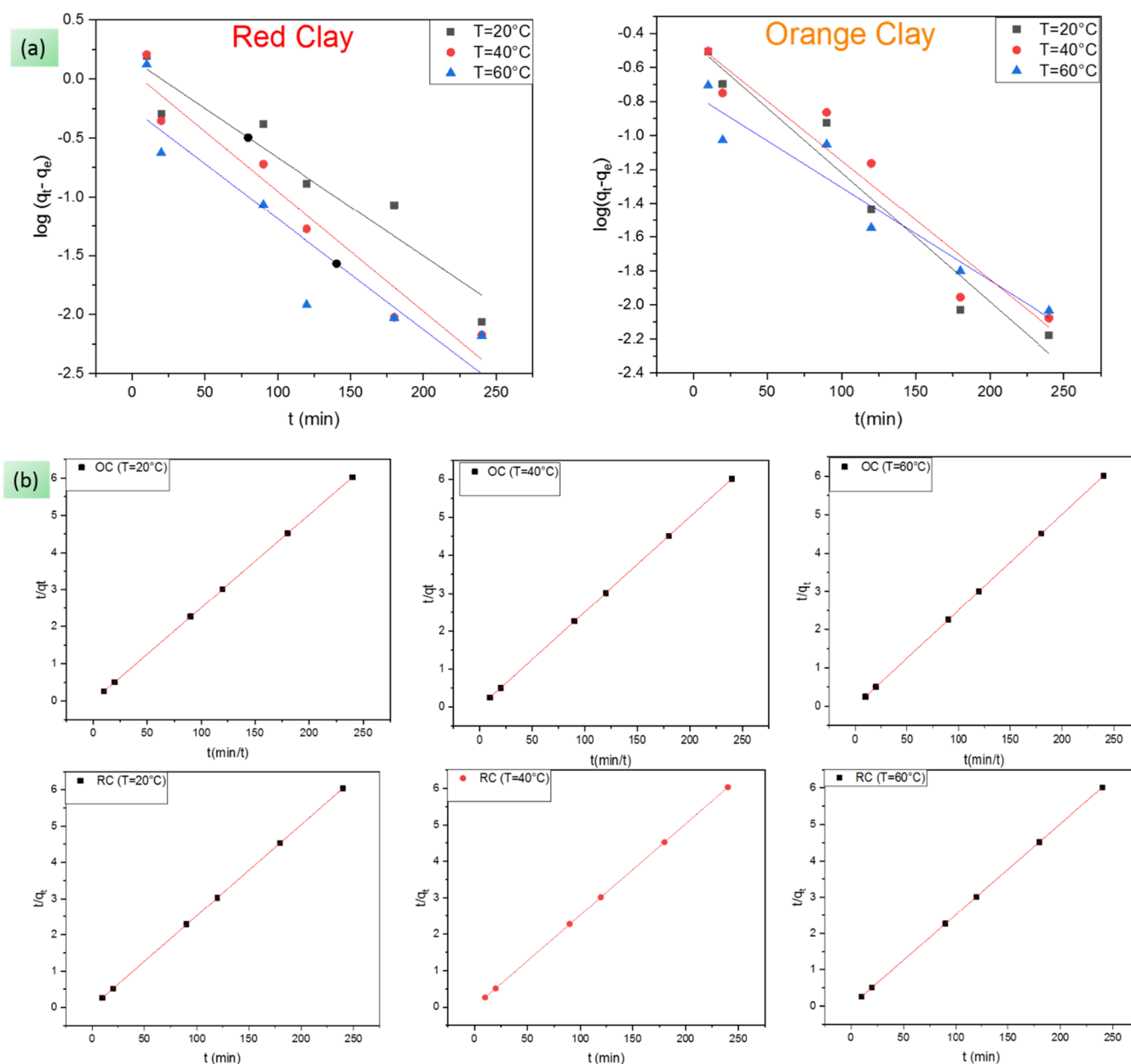where k_2 is the pseudo-second-order rate constant (g·mg^{-1}·min^{-1}), A is the pre-exponential factor (min^{-1}), R is the gas

Figure 7. Representation of the pseudo-first-order model (a) and the pseudo-second-order model (b).

constant (8.314 J·mol^{-1}·K^{-1}), T the adsorption temperature (K), and E_a is the apparent activation energy of the adsorption (Kj·mol^{-1}). By plotting Ln (k_2) versus $1/T$ (the Figure is not shown), the slopes lead to E_a values for MB adsorption onto RC and OC which are 49.63 and 11. 62 kJ·mol^{-1}, respectively. The activation energy range is less than 50 kJ·mol^{-1}, suggesting a physisorption mechanism. Indeed, when the rate is controlled by the film diffusion mechanism, the activation energy is very low (less than 40 kJ·mol^{-1}).

3.2.2. pH Effect. The pH of the aqueous solution is an important factor in the adsorption of any molecule. The adsorption capacity of OC and RC showed a progressive increase in the amount of MB retained with an increase in pH (Figure 9).

These results can be explained by the point of zero charge (pzc). The pH$_{pzc}$ of red clay RC and orange clay OC are, respectively, 7.97 and 8.98. Thus, at higher pH values, A negative charge exists at the surface, while the surface is positively charged at pH levels between 7.97 and 8.98. The increased adsorption of methylene blue (MB) in basic media is thus explained by the electrostatic attraction between the surface of the negatively charged adsorbent and the positively charged MB molecules.[26−33]

3.3. Adsorption Isotherm. MB adsorption isotherm experiments on RC and OC were studied in the initial concentration range from 20 to 300 mg·L^{-1}. The aim was to determine the best adsorbent by providing information on the adsorbent/adsorbate affinity and an understanding of the energy of the bonds between the adsorbate and the adsorbent. The experimental points obtained are represented in Figure 10, which shows the evolution of the adsorbed quantity of MB as a function of the residual concentration at different temperatures (20−60 °C).

Similarly for the kinetic studies, the impact of starting concentration was studied using linear versions of the Langmuir and Freundlich models. Parameter values resulting from these
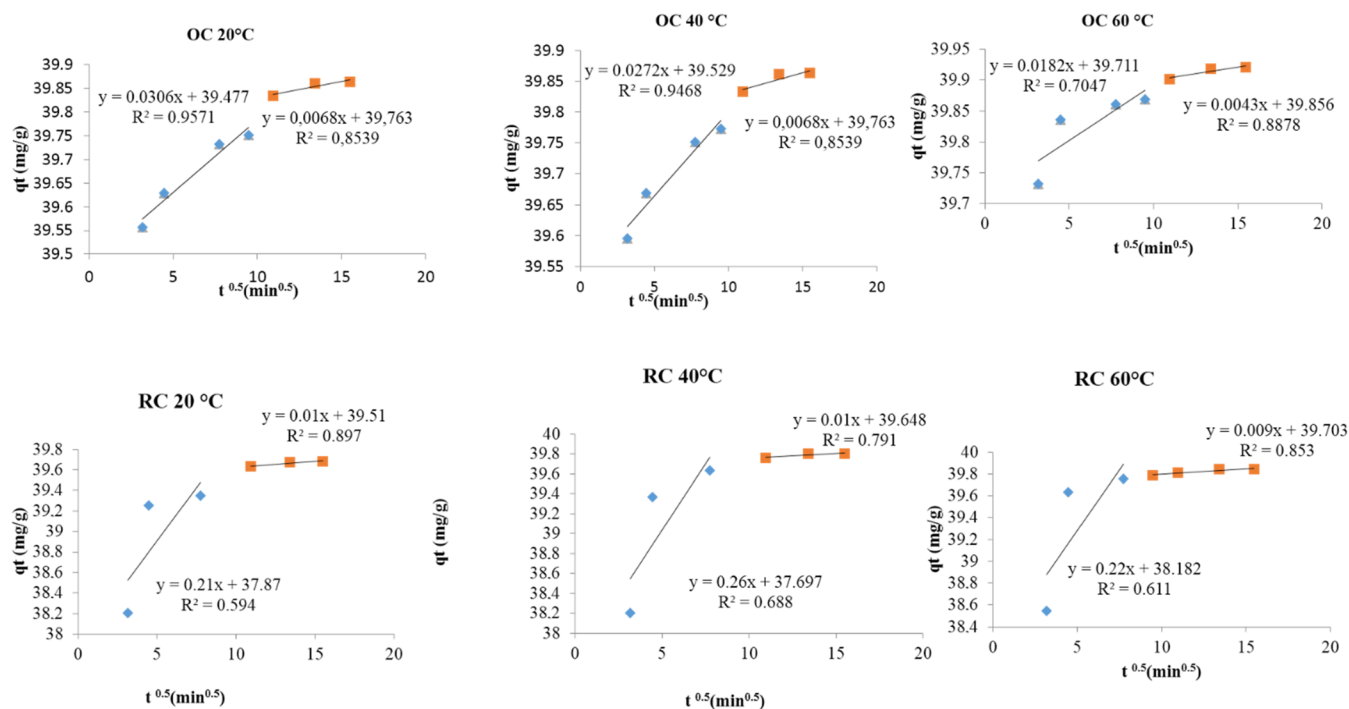
Figure 8. Intraparticle diffusion model for adsorption of MB on the OC and RC.

Table 3. Intraparticle Diffusion Model Parameters

temperature T (°C)	red clay (RC)				orange clay (OC)			
	K_3 (mg/gmin$^{0.5}$)	R^2	K'_3 (mg/gmin$^{0.5}$)	R^2	K_3 (mg/gmin$^{0.5}$)	R^2	K'_3 (mg/gmin$^{0.5}$)	R^2
$T = 20$ °C	0.207	0.594	0.011	0.896	0.030	0.957	0.006	0.853
$T = 40$ °C	0.267	0.687	0.010	0.791	0.027	0.946	0.006	0.853
$T = 60$ °C	0.220	0.610	0.009	0.853	0.018	0.704	0.004	0.887
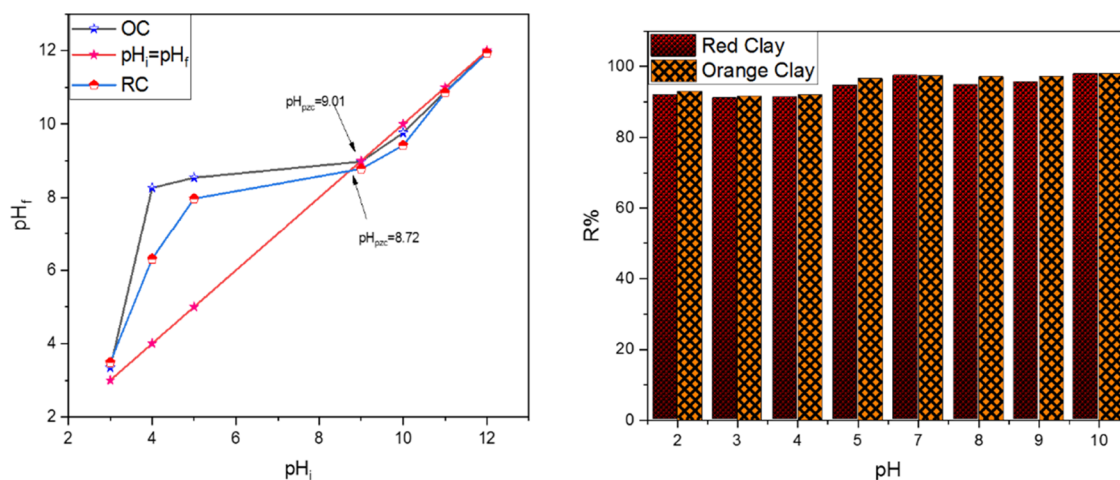
Figure 9. pH$_{pzc}$ and R% of the OC and RC.

models are reported in Table 4, and the linear curves of these models at different temperatures are shown in Figures 11 and 12. In addition, linear modeling was performed to determine the best model to represent the adsorption isotherms of MB on the two clays. The R^2 values for MB adsorption show that the two clays behave similarly (Table 4). Adsorption of MB on both adsorbents was well-correlated with the Langmuir model over the examined temperature and concentration ranges, suggesting that adsorption sites on the surface are energetically

homogeneous and that the adsorption process occurs in a monolayer.[34−36]

The parameters calculated using the Langmuir and Freundlich models for MB are presented in Table 4. According to these results, orange clay is the most effective clay for eliminating MB with an adsorption capacity (79.61 mg·g^{-1}) greater than that of red clay (67.79 mg·g^{-1}), the K_F values increase, and the parameter $1/n$ is less than unity, which indicates that the adsorption affinity of the two solids is favorable to MB.[38]
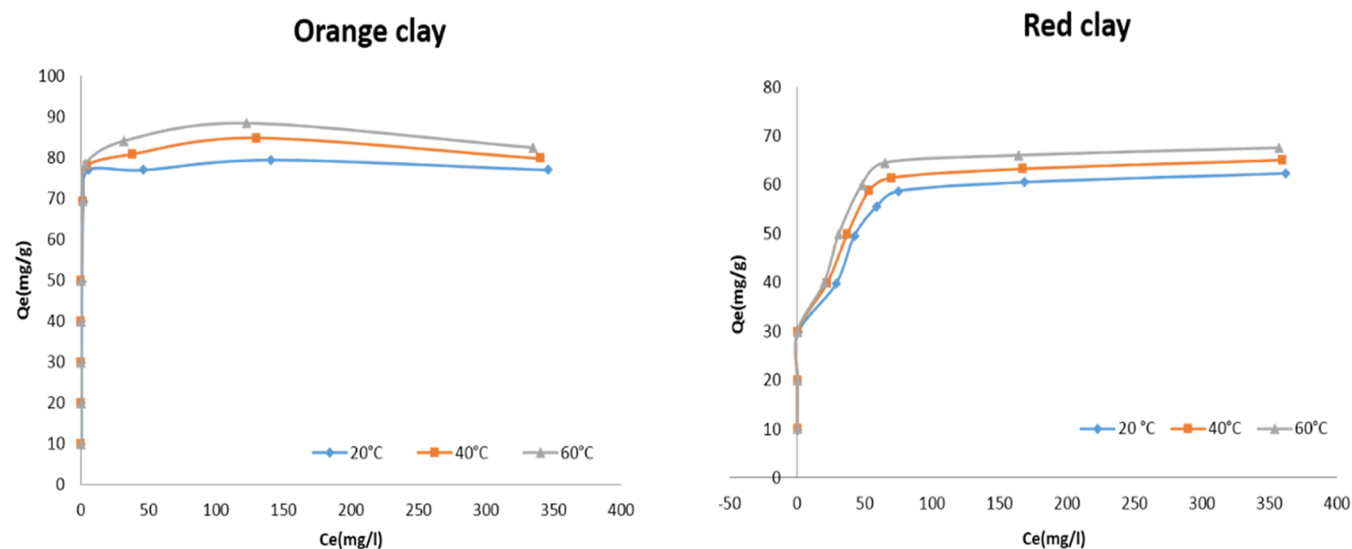
Figure 10. MB adsorption isotherms for clays: orange clay and red clay.

Table 4. Langmuir and Freundlich Parameters for MB at Different Temperatures

		Langmuir			Freundlich			
	temperature	K_L (L·mg^{-1})	Q_{max}(mg·g^{-1})	R^2	K_F (L·mg^{-1})	$1/n$	n	R^2
red clay	20 °C	1.05	77.76	0.998	47.436	0.058	17.185	0.854
	40 °C	0.60	80.06	0.999	48.043	0.064	15.479	0.894
	60 °C	0.33	88.65	0.999	48.300	0.068	14.652	0.068
orange clay	20 °C	1.73	79.61	0.999	46.01	0.062	16.180	0.891
	40 °C	1.37	84.96	0.999	47.41	0.067	14.940	0.933
	60 °C	1.35	88.65	0.999	48.27	0.069	14.510	0.934

3.4. Adsorption Thermodynamics. Adsorption of the MB on the OC and RC was analyzed using the following relations to calculate standard thermodynamic parameters, including enthalpy (ΔH), entropy (ΔS), and Gibbs free energy (ΔG)

$$\ln K_d = \frac{\Delta S°}{R} - \frac{\Delta H°}{RT} \tag{9}$$

where the values for R (8.314 J·K^{-1}·mol^{-1}), K_d (L·mg^{-1}), and T (K) for the values of the gas constant and solution temperature, respectively.

Straight lines with slope ΔH can be obtained by plotting Ln (K_d) vs $1/T$ (not shown in Figure 13).

Table 5 summarizes the values of $\Delta H°$, $\Delta S°$, and $\Delta G°$. Positive values of $\Delta H°$ and $\Delta S°$, respectively, indicate the endothermic nature which corresponds to the adsorption isotherm, and a good affinity of BM toward the two clays. The values of $\Delta H°$ (<40 kJ mol^{-1}) indicate that MB adsorption on both solids is physical in nature, while those of $\Delta S°$ show that MB molecules were more ordered on RC than on OC. The negative values of $\Delta G°$ indicate that the MB adsorption process is spontaneous and that its adsorption is more favorable at higher temperatures on both solids. Similar findings in other studies have also revealed that the adsorption of cationic dyes on clays is spontaneous and endothermic.[22,23]

3.5. Adsorption Mechanism. Figure 14 shows how the natural clay may change the MB dye if exposed to it. The adsorption process is influenced by the morphology of the clay as well as the functional activity and selectivity of the MB dye molecule.

The flat structure of clay makes it ideal for adsorption of the organic dye adsorbent via van der Waals forces and heteroatomic interactions. The adsorption phenomenon is unusual in that it depends on the strength of electrostatic contacts.[37,38]

3.5.1. DFT Study. Methylene blue was drawn by the use of Avogadro software[39,40] and geometrically optimized using MOPAC2016[41] via the PM6 semiempirical model. The MOPAC output was optimized via the use of Gaussian'16 software via the use of B3LYP/6-311+G(d,p)[42−45] level of theory. The highest occupied and lowest unoccupied molecular orbitals (HOMO and LUMO) and their energies and the Mulliken charges and NPA charges were extracted using the Gauss view program.[46]

According to Figure 15b,c, it can be seen that the electron densities of both the HOMO and LUMO surfaces are concentrated overall in the molecular moiety of the MB, indicating that there is a charge transfer due to the delocalization of the π-electrons. These results indicate that MB has different electron-rich and electron-poor regions, which makes its removal expected by either calcite or SiO$_2$. Molecular electrostatic potential map (Figure 15d) provides a detailed qualitative map of the locations responsible for nucleophilic and electrophilic assaults (areas rich in electrons and areas low in electrons, respectively). The given map is identified by the color grade, which is switched from negative to positive potential as follows: red (−ve) < orange < green < blue (+Ve) color (Figure 15d). The strong red color characterizes the electron-rich regions, while the strong blue color characterizes the electron-poor regions.[47−51] The dark brown color in the middle part of the map corresponds to the chloride ion. Inspection of the ESP map indicates that the nitrogen atoms as well as some carbon atoms
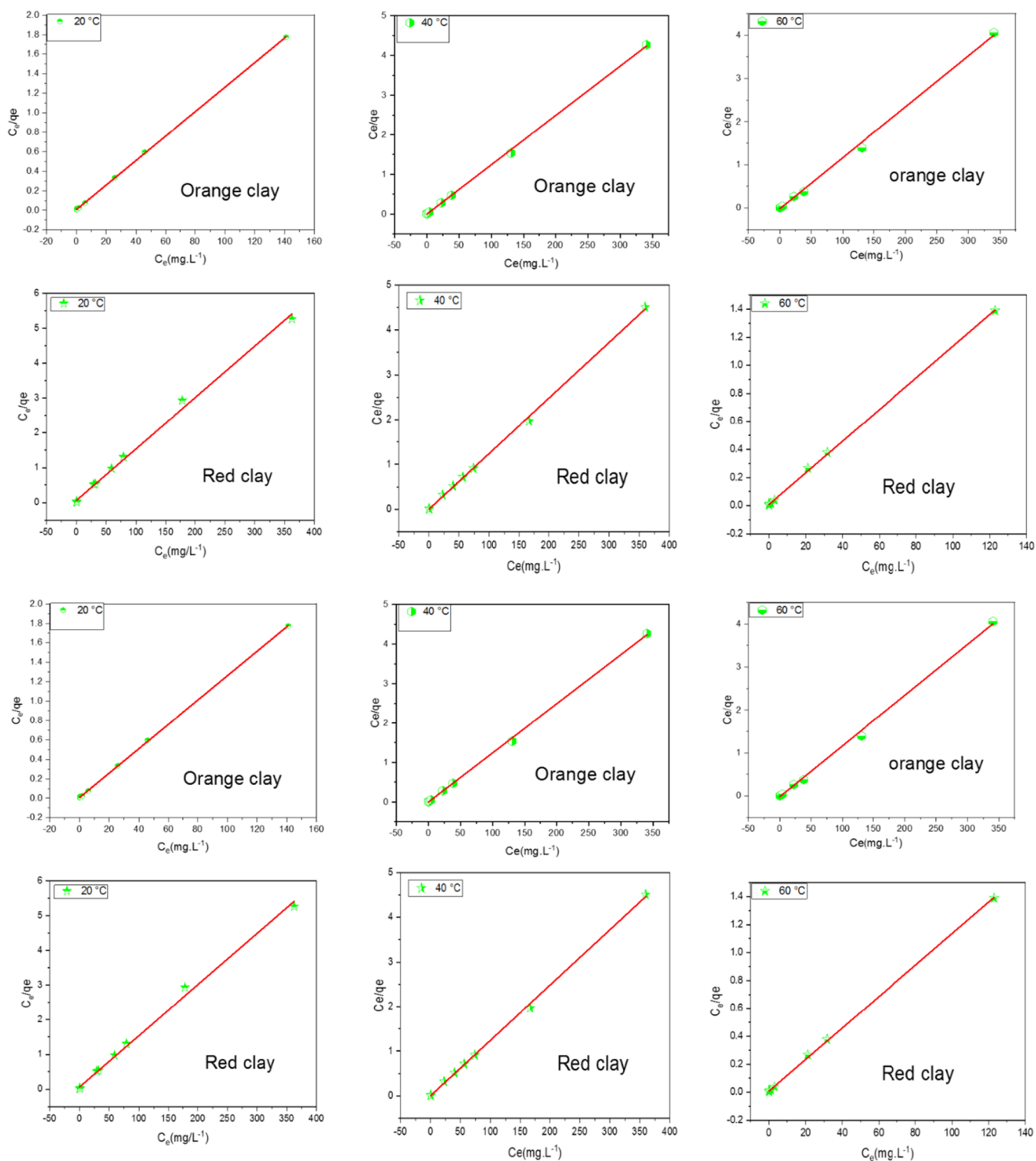
Figure 11. Langmuir isotherm for MB adsorption onto clay.

when located in the delocalized π-electron region of the two phenyl groups are mapped with red color, indicating that these regions are responsible for electrophilic attacks. Whereas, the sulfur atom and some of carbon atoms in the two phenyl groups are mapped with blue color, signifying that these parts of the molecules are responsible for nucleophilic attacks. These results can be also visualized and confirmed by looking at the total-density map at HOMO and LUMO (Figure 15e,f). These results

are also confirmed by mapping the charge distribution. The full set of numerical mulliken and NBO charges is listed in Table 6.

The energy gap and some global quantum chemical descriptors of MB are also shown in Figure 15h. As can be seen in the figure, the MB dye is characterized by a high value of HOMO and a low value of LUMO, which makes the ability to donate or accept electrons to or from the surface very high. The small energy gap of the MB (2.522 eV) indicates the high chemical reactivity and the kinetic instability of the MB
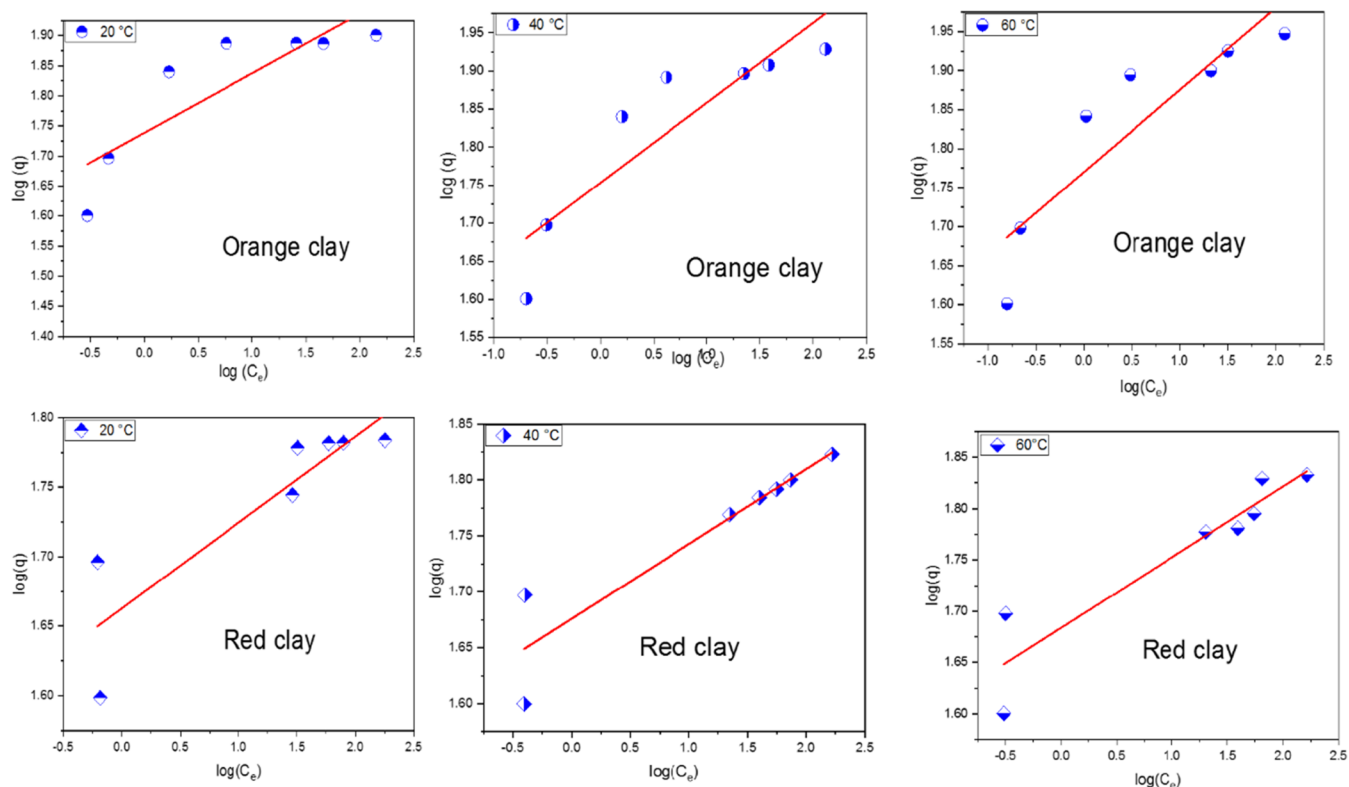
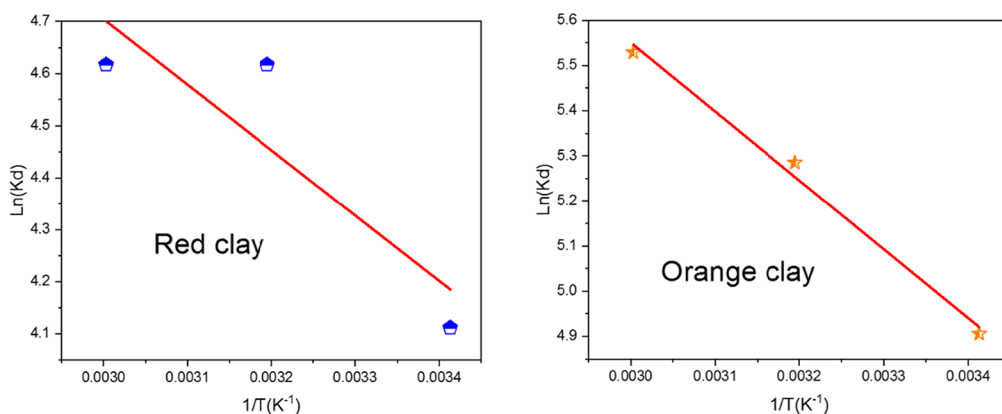**Figure 12.** Freundlich isotherm for the adsorption of MB onto clay.

Figure 13. Van't Hoff presentation of the MB adsorption curve on the clay's RC and OC.

Table 5. Thermodynamic Parameters for the Adsorption of MB on RC and OC

clay	T	$\Delta S°(\text{J·K}^{-1}\text{·mol}^{-1})$	$\Delta H°$ $(\text{J·mol}^{-1}\text{·K}^{-1})$	R^2	$\Delta G(\text{kJ·mol}^{-1})$
RC	20 °C	70.49	10.45	0.781	−7.97
	40 °C				−9.38
	60 °C				−10.7
OC	20 °C	84.19	12.68	0.992	−1.19
	40 °C				−1.36
	60 °C				−1.53

molecule. Moreover, the excitation process is permitted due to the high contact between HOMO and LUMO.

3.5.2. Molecular Dynamics (MD) and Monte Carlo (MC) Simulations. To comprehensively investigate the complex interaction between MB (methylene blue) molecules and a simulated clay surface, the utilization of Monte Carlo (MC) simulations proved to be absolutely crucial. These computa-

tional simulations involved the examination of two distinct types of surfaces, represented as spherical nanoclusters with a diameter of 12 Ångströms: (1) SiO_2−OH and (2) calcite (as illustrated in Figure 16a). These surfaces were immersed in an adsorption environment containing a single MB molecule along with 2500 water molecules. These simulations played a pivotal role in enabling us to thoroughly explore the dynamic behavior
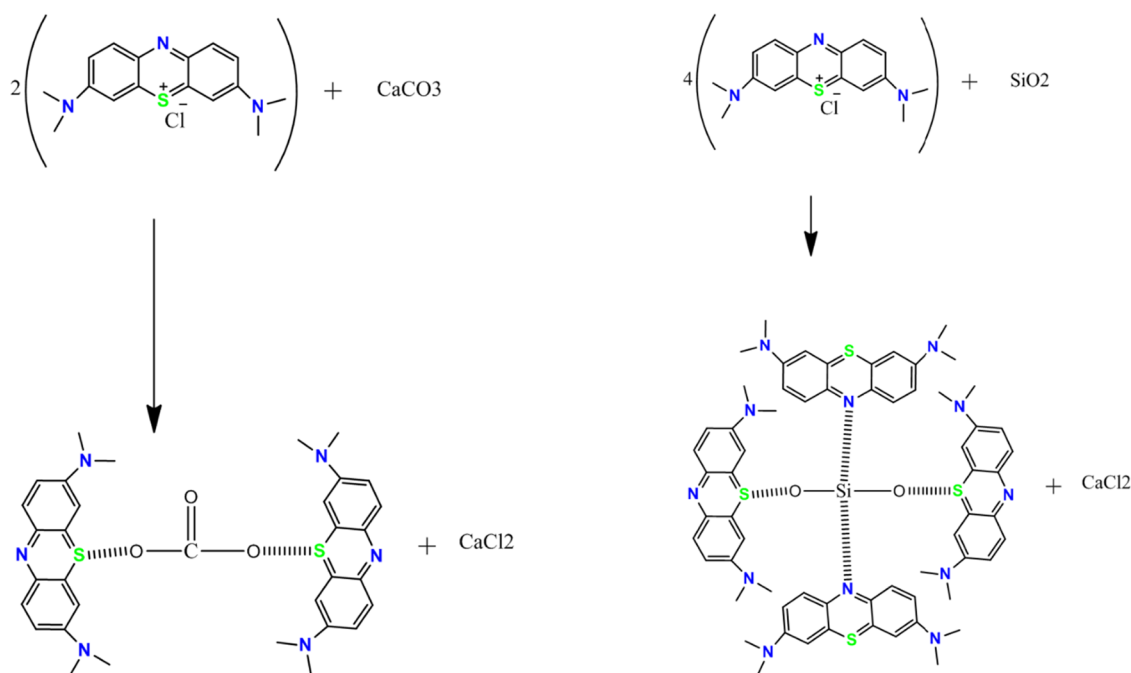
Figure 14. Electrostatic and ionic interactions between MB dye and two different clay adsorbents.
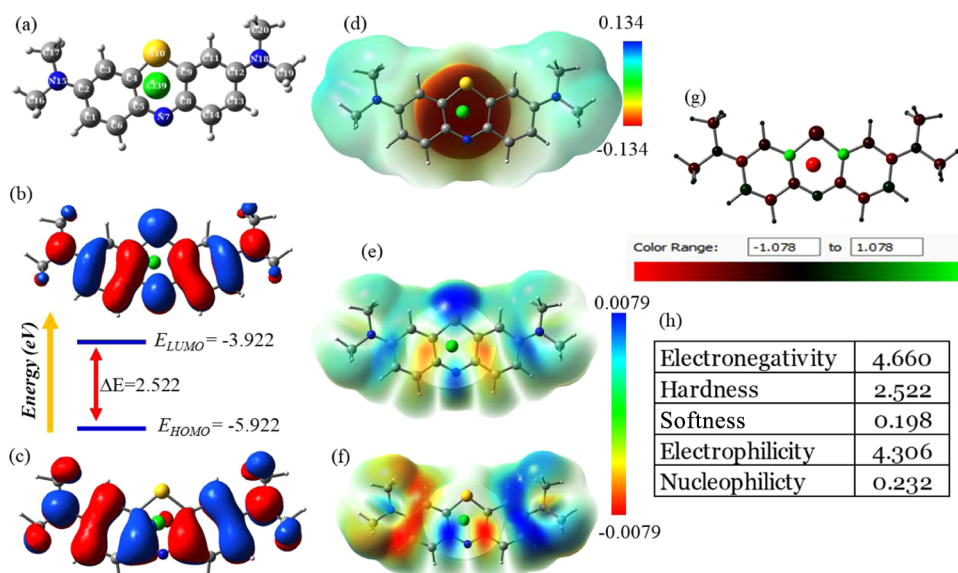

Figure 15. (a) Optimized structure, (b) electron density distribution of HOMO, (c) electron density distribution of LUMO, (d) electrostatic potential map, (e) total density at the HOMO surface, (f) total density at the LUMO surface, (g) Mulliken charge distribution, and (h) table of most relevant global descriptors of the methylene blue dye calculated at B3LYO/6-311+g(d,p)//PM6 in aqueous solution.

of molecules[52−54] and their binding characteristics with MB on both surface models. As a result, they provided invaluable insights into the intricate nature of these interactions, significantly advancing our understanding of how MB is adsorbed onto clay surfaces.[52] This knowledge serves as a foundation for further research in the field, enhancing our grasp of the underlying mechanisms at play.

The simulation's MC (Monte Carlo) and MD (molecular dynamics) computations made use of the well-established deriding force field,[55−58] renowned for its adaptability and proven reliability in scientific applications. In the MD simulations, we employed the NVT ensemble, maintaining a temperature of 298 K, which ensured the stability of the system

and closely mirrored real-world conditions. This MD simulation extended over a substantial duration of 1000 ps, affording us the opportunity to delve deeply into the intricate molecular dynamics and interactions within the system over an extensive time frame, as documented in references.[49,59−61] Through these rigorous calculations, we gained a comprehensive understanding of how the system behaved and its properties under the specified conditions, as elucidated in references.[62−64] This thorough exploration of the system's behavior enhances our ability to interpret and apply the results in various scientific contexts.

3.5.3. Molecular Dynamics and Monte Carlo Simulations. Determining the best setup for adsorption of MB (methylene blue) molecules in order to accurately measure the different

Table 6. Natural Population Atomic (NPA) Charges and Mulliken Charges of the MB Molecule

atom	NPA	MC	atom	NPA	MC
C1	−0.2386	0.1381	C11	−0.2768	−0.1923
C2	0.2533	−0.4720	C12	0.2519	−0.4595
C3	−0.2789	−0.1833	C13	−0.2476	0.1249
C4	−0.1415	0.9891	C14	−0.1144	−0.4217
C5	0.1164	−0.2840	N15	−0.3926	0.0200
C6	−0.1309	−0.4136	C16	−0.3666	−0.3021
N7	−0.3617	0.1321	C17	−0.3670	−0.3011
C8	0.1046	−0.3468	N18	−0.3944	0.0218
C9	−0.1516	0.9462	C19	−0.3673	−0.3068
S10	0.5416	−0.3128	C20	−0.3665	−0.3080
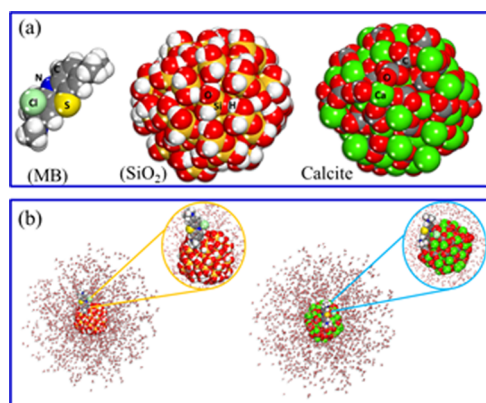
Figure 16. (a) Optimized structures for MB, SiO_2, and calcite nanocluster and (b) the adsorption of MB onto the SiO2 and calcite contact was analyzed using MC and MD to determine the lowest energy geometries.

energy outputs, we need to know which would lead to the most efficient adsorption process. Important to this study is how the adsorbate molecule interacts with the clay interface, here represented by SiO_2 and calcite. Insights regarding the system's energetics and stability can be gleaned from this interaction, making it a veritable treasure trove of data. Adsorption energy associated with this approach can be calculated by analyzing this complex interplay, which is a critical piece of the puzzle. These adsorption energies serve as key indicators, shedding light on the underlying mechanisms governing the system's behavior.[53,54,65] They are also crucial in leading the way for the development of effective adsorption strategies on clay surfaces, not only for MB but for molecules with similar characteristics as shown in Figure 17a. To quantitatively determine the adsorption energy (E_{ads}), we can employ the following equation:[49,66−68]

$$E_{ads} = E_{total} - (E_{clay} + E_{MB} + E_{water}) \tag{10}$$

where E_{ads} represents the adsorption energy, E_{total} is the total energy of the system, E_{clay} signifies the energy of the clay surface, E_{MB} denotes the energy of the MB molecule, and E_{water} represents the energy of the surrounding water molecules. By solving this equation, we are equipped with a precise measure of the adsorption energy, which is instrumental in unraveling the intricate dynamics of the adsorption process.[52,64,69,70]

The approach we employed, known as Monte Carlo (MC), to evaluate the intricacies of molecular interactions, entails the generation of a multitude of combinations involving species relevant to the simulation, such as molecules and ions. These combinations are generated randomly, allowing for a thorough exploration of a wide array of configurations, as elaborated in refs 60,66,71,72. In Figure 17a, we present the adsorption geometries of the adsorbate molecules, emphasizing their proximity to the SiO_2 and calcite interfaces. This proximity results in robust interactions, which in turn give rise to notably large negative adsorption energies, as visualized in Figure 17b.[59,71] Adsorption energies are strongly negative, suggesting that MB molecules have a high affinity for the interface and are quite stable there. These results give us important information about how adsorption behaves, shedding light on the intricate dynamics governing the interactions between MB and SiO_2 as well as calcite surfaces. It deepens our understanding of how MB molecules engage with these surfaces, ultimately contributing to the body of knowledge surrounding this important process.

Adsorbed adsorbate molecules on SiO_2 and calcite surfaces showing a considerable increase in negative E_{ads} values is indicative of adsorbate molecules' strong binding to and preferential adsorption by adsorbent surfaces.[60,61,73,74] The data presented here lend credence to the hypothesis that the adsorbent serves as a superior substrate for efficient adsorption, which may result in greater adsorption capacities and better
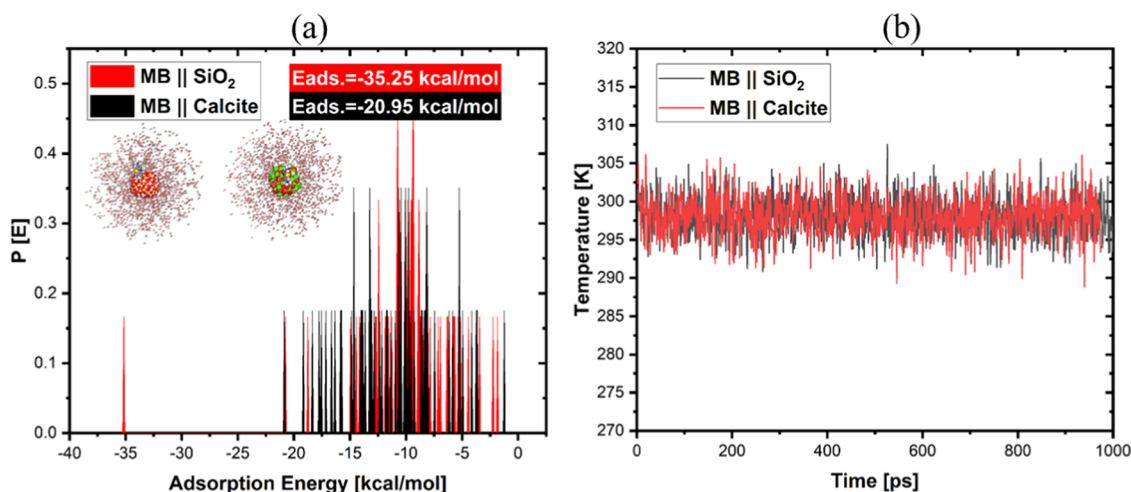
Figure 17. MD run's effect on the MB molecule's adsorption temperatures on SiO_2 and calcite (**a**) and the adsorption energy probability distribution (**b**).

performance in appropriate uses.[66] Since there was only a little amount of temperature drift during the MD simulation, we may be confident that our results will hold up (Figure 17b).[59−61,75]

The simulations are more credible and valid since they coincide with experimental observations. With the MB molecules' effective adherence to the surfaces as a starting point, a consistent and accurate picture of the MB-surface interactions may be constructed. Our study's well regulated temperature conditions were crucial in allowing for a detailed analysis of molecule motion and interaction. Our confidence in the accuracy of the data we've collected and in the validity of the observations we've made, thanks to the small temperature swings we've seen, is further bolstered by the fact that they're consistent with the simulation's predictions, as shown in the supporting refs 65,68,76. These results, which are substantiated in references, add substantially to our understanding of the behavior and attributes of the system under the conditions we simulated.[66,68,77,78] Moreover, computation of the relative concentration of MB (methylene blue) on the respective surfaces, as illustrated in Figure 16b, lends additional support to our findings. This analysis reveals a notable affinity of MB molecules for the surfaces, demonstrating their effective adhesion. Our simulations are further validated and strengthened by the agreement between our computer results and experimental data. Our experimental results are supported by the fact that MB molecules adhere well to the surfaces in issue; this allows us to make sense of the complex interactions between MB and the surfaces in question. This convergence between computational and experimental data enhances the comprehensiveness and reliability of our research, providing a robust basis for further exploration in this field. In a broader context, these findings exemplify the synergy between theoretical and experimental methodologies, demonstrating how they can work harmoniously to advance our understanding of complex phenomena like adsorption. By providing strong corroborative evidence, our results showcase the immense value of computational techniques in refining and validating experimental data, thereby enriching our comprehension of intricate processes such as MB adsorption. This symbiotic relationship between theory and experimentation signifies a powerful approach in advancing scientific knowledge and solving real-world challenges. It serves as a testament to the interdisciplinary nature of modern scientific investigation, where computational tools and experimental techniques collaborate to push the boundaries of our understanding.[49,54,59,61,79−83]

4. CONCLUSIONS

The study investigating the adsorption of methylene blue (MB) from aqueous solutions using clay micrographs revealed a clay raw material with a variable surface magnification, suggesting a desired multiphase structure for the adsorbents.

After the adsorption of the MB dye to the clay, an EDX spectrum was taken, revealing a chlorine signal and indicating that the dye had undergone a complex reaction. Prominent diffraction lines in the raw clay identified calcite, quartz, rutile sodium, and magnetite. $CaSiO_3$ (calcium silicate) was detected by the FX method. At a pH of 6.5 and a clay concentration of 0.02 g, adsorption equilibrium was reached after 180 min.

As a result, the dye molecules are more ordered on the adsorbent than in the solution, and the endothermic nature of MB adsorption on the clay is proven, as shown by the negative value of (ΔH^0) and the positive value of (ΔS^0). Adsorption is a spontaneous process, where the activation energy is negative

(ΔG^0). For MB concentrations ranging from 80 mg·L^{-1}, the adsorption capacity varies from the various temperature adsorbed for OC at T = 20, 40, and 60 °C are 39.86, 39.39, and 39.92 mg·g^{-1}, respectively, and for CR are 39.76, 39.81, and 39.87 mg·g^{-1}, respectively. Pseudo-second-order kinetics is used to investigate MB adsorption. The Langmuir isotherm, with a higher R^2 correlation, provides a more accurate description of the adsorption process for our clays compared to the Freundlich isotherm. DFT results showed that the MB molecule has different sites that are able to donate to accept electrons from or to the adsorbate surface.

In essence, the paramount objective lies in pinpointing the most optimal adsorption arrangement for the MB (methylene blue) molecule. Achieving this precision is essential for accurately determining diverse energy outcomes and ensuring an efficient adsorption process. The success of our investigation depends on how the adsorbate molecule interacts with the clay contact, which is represented by SiO_2 and calcite structures. Adsorption energies may be evaluated and calculated, thanks to this interaction, providing essential insight into the energetics and stability of the system as a whole. These findings are important because they provide light on the mechanisms at play and will help researchers design effective methods of adsorbing MB and similar chemicals onto clay surfaces.

We employ the Monte Carlo (MC) method to create numerous species combinations for our simulations, enabling a comprehensive analysis of various scenarios. The observed significant interactions and large negative adsorption energies strongly suggest high affinity and durability of MB molecules at the interface. Correlating our simulation results with experimental findings enhances the credibility of our simulations. This involves computational analysis of the MB concentration and monitoring temperature changes during molecular dynamics (MD) simulations. The alignment of the experimental and computational data bolsters our confidence in our results. This integrated approach highlights the crucial role of computational tools in enhancing our understanding of MB adsorption. It demonstrates how computational methods can effectively complement experimental research, creating a synergy that furthers our knowledge and practical applications in this domain.

■ AUTHOR INFORMATION

Corresponding Authors

Jaouad Bensalah − *Laboratory of Advanced Materials and Process Engineering (LAMPE), Department of Chemistry, Faculty of Sciences, Ibn Tofaïl University, 14000 Kenitra, Morocco*; Email: Jaouad.bensalah@uit.ac.ma

Musaab Dauelbait − *Department of Scientific Translation, University of Bahri, Bahri 11111, Sudan*; orcid.org/0009-0003-0685-8243; Email: musaabelnaim@gmail.com

Authors

Sarra Sellak − *Laboratory of Advanced Materials and Process Engineering (LAMPE), Department of Chemistry, Faculty of Sciences, Ibn Tofaïl University, 14000 Kenitra, Morocco*

Hanae Ouaddari − *Laboratory of Advanced Materials and Process Engineering (LAMPE), Department of Chemistry, Faculty of Sciences, Ibn Tofaïl University, 14000 Kenitra, Morocco; Chemistry platform, UATRS, National Center for Scientific and Technical Research (CNRST), Rabat 10500, Morocco*

Zaki Safi − *Chemistry Department, Faculty of Science, Al Azhar University-Gaza, 1277 Gaza, Palestine*

Avni Berisha − *Department of Chemistry, Faculty of Natural and Mathematics Science, University of Prishtina, 10000 Prishtina, Kosovo*

Khalid Draoui − *Laboratory MSI, Faculty of Sciences, Abdelmalek Essaadi University, Tetouan 93030, Morocco*

Ilias Barrak − *Hydrogen Solutions - INNOVX, University Mohammed VI Polytechnic, Ben Guerir 43150, Morocco*

Taoufiq Guedira − *Laboratory of Organic Chemistry, Catalysis, and Environment, University of Ibn Tofail, Faculty of Science, Kenitra 14000, Morocco*

Mohammed Bourhia − *Department of Chemistry and Biochemistry, Faculty of Medicine and Pharmacy, Ibn Zohr University, Laayoune 70000, Morocco; Laboratory of Chemistry-Biochemistry, Environment, Nutrition, and Health, Faculty of Medicine and Pharmacy, University Hassan II, B. P. 5696 Casablanca, Morocco;* ⊙ orcid.org/0000-0003-3707-8461

Samir Ibenmoussa − *Laboratory of Therapeutic and Organic Chemistry, Faculty of Pharmacy, University of Montpellier, Montpellier 34000, France*

Mohammad Okla − *Botany and Microbiology Department, College of Science, King Saud University, Riyadh 11451, Saudi Arabia*

Amar Habsaoui − *Laboratory of Advanced Materials and Process Engineering (LAMPE), Department of Chemistry, Faculty of Sciences, Ibn Tofaïl University, 14000 Kenitra, Morocco*

Mohamed Harcharras − *Laboratory of Advanced Materials and Process Engineering (LAMPE), Department of Chemistry, Faculty of Sciences, Ibn Tofaïl University, 14000 Kenitra, Morocco*

Complete contact information is available at:
https://pubs.acs.org/10.1021/acsomega.3c09536

Author Contributions

Conceptualization, original draft—writing, reviewing, and editing: S.S., J.B., H.O., Z.S., and A.B. Formal analysis, investigations, funding acquisition, reviewing, and editing: K.D., I.B., T.G., and M.B. Resources, data validation, data curation, and supervision: S.I., A.M.K.O., A.H., and M.H..

Notes

The authors declare no competing financial interest.

■ REFERENCES

(1) Khan, S.; Malik, A. Environmental and health effects of textile industry wastewater. In *Environmental Deterioration and Human Health*; Springer, 2014; pp 55−71.

(2) Manzoor, J.; Sharma, M. Impact of textile dyes on human health and environment. In *Impact of Textile Dyes on Public Health and the Environment*; IGI Global, 2020; pp 162−169.

(3) Lebkiri, I.; Abbou, B.; Kadiri, L.; Ouass, A.; Essaadaoui, Y.; Habssaoui, A.; Rifi, E. H.; Lebkiri, A. Removal of methylene blue dye from aqueous solution using a superabsorbant hydrogel the polyacrylamide: isotherms and kinetic studies. *Mediterr. J. Chem.* **2019**, *9* (5), 337−345.

(4) Weng, C. H.; Pan, Y. F. Adsorption of a cationic dye (methylene blue) onto spent activated clay. *J. Hazard. Mater.* **2007**, *144* (1−2), 355−362.

(5) Robinson, T.; McMullan, G.; Marchant, R.; Nigam, P. Remediation of dyes in textile effluent: a critical review on current treatment technologies with a proposed alternative. *Bioresour. Technol.* **2001**, *77* (3), 247−255.

(6) Lebkiri, İ.; Abbou, B.; Kadiri, L.; Ouass, A.; ElamrÎ, A.; Ouaddari, H.; ElkhattabÎ, O.; Lebkiri, A.; RÎFÎ, E. H. Equilibrium, Kinetic Data, and Adsorptıon Mechanism for Lead Adsorptıon onto Polyacrylamıde Hydrogel. *J. Turkish Chem. Society, Section A: Chemistry* **2021**, *8*, 731−748.

(7) Hublik, G.; Schinner, F. Characterization and immobilization of the laccase from Pleurotusostreatus and its use for the continuous elimination of phenolic pollutants. *Enzyme Microb. Technol.* **2000**, *27*, 330−336, DOI: 10.1016/S0141-0229(00)00220-9.

(8) Ince, M.; Ince, O. K. An overview of adsorption technique for heavy metal removal from water/wastewater: a critical review. *Int. J. Pure Appl. Sci.* **2017**, *3* (2), 10−19.

(9) Kedi, A. B. B.; Kouassi, S. S.; Coulibaly, V.; Sei, J. Elimination de polluants des d'echets liquides d'une unit'e de production de sucre par des argiles naturelles de Côte d'Ivoire. *Int. J. Biol. Chem. Sci.* **2021**, *15* (2), 803−815.

(10) Romdhane, D. F.; Satlaoui, Y.; Nasraoui, R.; et al. Adsorption, Modeling, Thermodynamic, and Kinetic Studies of Methyl Red Removal from Textile- Polluted Water Using Natural and Purified Organic Matter Rich Clays as Low-Cost Adsorbent. *J. Chem.* **2020**, *2020*, No. e4376173.

(11) Feddal, I.; Mimanne, G.; Dellani, A.; et al. Synthèse et caractérisation d'un matériau adsorbant: Application to textile dye elimination. *Mater. Today: Proc.* **2022**, *49*, 981−985.

(12) Sorgho, B.; Guel, B.; Zerbo, L.; et al. A study of adsorption of cadmium, copper and lead by two clays from Burkina Faso. *Int. J. Biol. Chem. Sci.* **2019**, *12* (6), 2933−2950.

(13) Allaoui, M.; Berradi, M.; Bensalah, J.; Es-sahbany, H.; Dagdag, O.; Ibn Ahmed, S. Study of the adsorption of nickel ions on the sea shells of Mehdia: Kinetic and thermodynamic study and maJ.Bensa-lahthematical modelling of experimental data. *Mater. Today: Proc.* **2021**, DOI: 10.1016/j.matpr.2021.02.234.

(14) Goldberg, S. Competitive adsorption of arsenate and arsenite on oxides and clay minerals contribution from the george e. Brown jr., salinity laboratory. *Soil Sci. Soc. Am. J.* **2002**, *66*, 413−421, DOI: 10.2136/sssaj2002.4130.

(15) Akçay, G.; Yurdakoc, M. K. Nonyl-and dodecylamines intercalated bentonite and Illite from turkey. *Turk. J. Chem.* **1999**, *23*, 105−114.

(16) Pedro, G. *La classification des minéraux argileux (phyllosilicates): Étude historique et considérations critiques*; Institut National de la RechercheAgronomique, 1965.

(17) Hong, S.; Wen, C.; He, J.; Gan, F.; Ho, Y.-S. Adsorption thermodynamıcs of methylene blue onto bentonite. *J. Hazard. Mater.* **2009**, *167*, 630−633.

(18) Bellamy, L. J. *The infra-red Spectra of Complex Molecules*; Hall: London, 1975.

(19) Madejová, J.; Pálková, H. *NIR Contribution to the Study of Modified Clay Minerals Developments in Clay Science*; Elsevier, 2017; pp 447−481.

(20) El Hannafi, N.; Boumakhla, M. A.; Berrama, T.; Bendjama, Z. Elimination of phenol by adsorption on activated carbon prepared from the peach cores: modelling and optimization. *Desalination* **2008**, *223*, 264−268.

(21) Almeida, C. A. P.; Debacher, N. A.; Downs, A. J.; Cottet, L.; Mello, C. A. D. Removal of methylene blue from colored effluents by

adsorption on montmorillonite clay. *J. Colloid Interface Sci.* **2009**, *332*, 46−53.

(22) Elabboudi, M.; Bensalah, J.; Amri, A. E.; Azzouzi, N. E.; Srhir, B.; lebkiri, A.; Zarrouk, A.; Rifi, E. H. Adsorption performance and mechanism of anionic MO dye by the adsorbent polymeric Amberlite®IRA-410 resin from environment wastewater: Equilibrium kinetic and thermodynamic studies. *J. Mol. Struct.* **2023**, *1277*, No. 134789.

(23) El Kerdoudi, Z.; Bensalah, J.; Helli, H.; El mekkaoui, A.; EL Mejdoub, N. Investigation of the cationic dye methylene blue in the treatment of wastewater clay from Sidi-Kacem (Morocco): Kinetic and mathematical modelling of experimental data. *Mater. Today Proc.* **2023**, *72*, 3550−3555.

(24) Bensalah, J.; Berradi, M.; Habsaoui, A.; Allaoui, M.; Essebaai, H.; El Khattabi, O.; Lebkiri, A.; Rifi, E.-H. Kinetic and thermodynamic study of the adsorption of cationic dyes by the cationic artificial resin Amberlite®IRC50. *Mater. Today Proc.* **2021**, *45*, 7468−7472.

(25) Amri, A. E.; Bensalah, J.; Idrissi, A.; Lamya, K.; Ouass, A.; Bouzakraoui, S.; Zarrouk, A.; Rifi, E. H.; Lebkiri, A. Adsorption of a cationic dye (Methylene bleu) by Typha Latifolia: Equilibrium, kinetic, thermodynamic and DFT calculations. *Chem. Data Collect.* **2022**, *38*, No. 100834.

(26) Bensalah, J.; Habsaoui, A.; Abbou, B.; Kadiri, L.; Lebkiri, I.; Lebkiri, A.; Rifi, E. H. Adsorption of the anionic dye methyl orange on used artificial zeolites: kinetic study and modeling of experimental data. *Mediterr. J. Chem.* **2019**, *9*, 311−316.

(27) Bensalah, J.; Galai, M.; Ouakki, M.; Amri, A. E.; Hanane, B.; Habsaoui, A.; Khattabi, O. E.; Lebkiri, A.; Zarrouk, A.; Rifi, E. H. A combined experimental and thermodynamics study of mild steel corrosion inhibition in 1.0 M hydrochloric solution by the cationic polymer Amberlite®IRC-50 resin extract. *Chem. Data Collect.* **2023**, *43*, No. 100976.

(28) Bensalah, J.; Berradi, M.; Habsaoui, A.; et al. Adsorption of the orange methyl dye and lead (II) by the cationic resin Amberlite®IRC-50: Kinetic study and modeling of experimental data. *J. Chem. Soc. Pak.* **2021**, *43*, 535−535.

(29) Bensalah, J.; Benhiba, F.; Habsaoui, A.; Ouass, A.; Zarrouk, A.; Lebkiri, A.; El Khattabi, O.; Rifi, E. H. The adsorption mechanism of the anionic and cationic dyes of the cationic resin A®IRC-50, kinetic study and theoretical investigation using DFT. *J. Indian Chem. Soc.* **2022**, *99*, No. 100512.

(30) Amri, A. E.; Bensalah, J.; Essaadaoui, Y.; Lebkiri, I.; Abbou, B.; Zarrouk, A.; Rifi, E. H.; Lebkiri, A. Elaboration, characterization and performance evaluation of a new environmentally friendly adsorbent material based on the reed filter (Typha Latifolia): Kinetic and thermodynamic studies and application in the adsorption of Cd (II) ion. *Chem. Data Collect.* **2022**, *39*, No. 100849.

(31) Bensalah, J.; Amri, A. E.; Ouass, A.; Hammani, O.; Kadiri, L.; Ouaddari, H.; Mustapha, S. E.; Zarrouk, A.; lebkiri, A.; Srhir, B.; Rifi, E. H. Investigation of the cationic resin Am®IRC-50 as a potential adsorbent of Co (II): Equilibrium isotherms and thermodynamic studies. *Chem. Data Collect.* **2022**, *39*, No. 100879.

(32) Bensalah, J. Removal of the textile dyes by a resin adsorbent polymeric: Insight into optimization, kinetics and isotherms adsorption phenomenally. *Inorg. Chem. Commun.* **2024**, *161*, No. 111975.

(33) Yin, J.; Zhan, F.; Jiao, T.; Deng, H.; Zou, G.; Bai, Z.; Zhang, Q.; Peng, Q. Highly efficient catalytic performances of nitro compounds via hierarchical PdNPs-loaded MXene/polymer nanocomposites synthesized through electrospinning strategy for wastewater treatment. *Chin. Chem. Lett.* **2020**, *31*, 992−995.

(34) Tahir, H.; Sultan, M.; Akhtar, N.; Hameed, U.; Abid, T. Application of natural and modified sugar cane bagasse for the removal of dye from aqueous solution. *J. Saudi Chem. Soc.* **2016**, *20*, S115−S121.

(35) Yin, J.; Zhan, F.; Jiao, T.; Wang, W.; Zhang, G.; Jiao, J.; Jiang, G.; Zhang, Q.; Gu, J.; Peng, Q. Facile preparation of self-assembled MXene@Au@CdSnanocomposite with enhanced photocatalytic hydrogen production activity. *Sci. China Mater.* **2020**, *63*, 2228−2238.

(36) Bensalah, J.; Ouaddari, H.; Erdoğan, Ş.; Tüzün, B.; Gaafar, A-R. Z.; Nafidi, H.-A.; Bourhia, M.; Habsaoui, A. Cationic resin polymer

A®IRC-50 as an effective adsorbent for the removal of Cr(III), Cu(II), and Ag(I) from aqueous solutions: A kinetic, mathematical, thermodynamic and modeling study. *Inorg. Chem. Commun.* **2023**, *157*, No. 111272.

(37) Lee, C.; Yoon, J. Temperature dependence of hydroxyl radical formation in the hv/Fe3+/H2O2 and Fe3+/H2O2 systems. *Chemosphere* **2004**, *56*, 923−934.

(38) Lan, Y.-C.; Kamal, S.; Lin, C.-C.; Liu, Y.-H.; Lu, K.-L. Ultra-thin Zr-MOF/PVA/Melamine composites with remarkable sound attenuation effects. *Microporous Mesoporous Mater.* **2023**, *360*, No. 112668.

(39) Hanwell, M. D.; Curtis, D. E.; Lonie, D. C.; Vandermeersch, T.; Zurek, E.; Hutchison, G. R. Avogadro: An Advanced Semantic Chemical Editor, Visualization, and Analysis Platform. *J. Cheminform.* **2012**, *4*, No. 17.

(40) Avogadro. *Free Cross-Platform Molecular Editor - Avogadro, (n.d.)* https://avogadro.cc/ (accessed 2024-02-16).

(41) Stewart, J. J. P. Optimization of Parameters for Semiempirical Methods VI: More Modifications to the NDDO Approximations and Re-Optimization of Parameters. *J. Mol. Model.* **2013**, *19*, 1−32.

(42) Mohammad-Salim, H.; de Julián-Ortiz, J. V. Theoretical insight into the mechanism and selectivity of the [3 + 2] cycloaddition reaction of N-methyl-1-phenylmethanimine oxide and bicyclopropylidene from the MEDT perspective. *Struct. Chem.* **2024**, *35*, 541−551.

(43) Singh, I.; Al-Wahaibi, L. H.; Srivastava, R.; Prasad, O.; Pathak, S. K.; Kumar, S.; Parveen, S.; Banerjee, M.; El-Emam, A. A.; Sinha, L. DFT Study on the Electronic Properties, Spectroscopic Profile, and Biological Activity of 2-Amino-5-Trifluoromethyl-1, 3, 4-Thiadiazole with Anticancer Properties. *ACS Omega* **2020**, *5*, 30073.

(44) Becke, A. D. Density-Functional Exchange-Energy Approximation with Correct Asymptotic Behavior. *Phys. Rev. A* **1988**, *38*, 3098.

(45) Becke, A. D. Density-functional Thermochemistry. IV. A New Dynamical Correlation Functional and Implications for Exact-exchange Mixing. *J. Chem. Phys.* **1996**, *104*, 1040.

(46) Dennington, R.; Keith, T. A.; Millam, J. M. *GaussView 6.0. 16*; Semichem Inc.: Shawnee Mission. KS, USA, 2016.

(47) Abdel-Mottaleb, M. S. A.; Ali, S. N. A New Approach for Studying Bond Rupture/Closure of a Spiro Benzopyran Photochromic Material: Reactivity Descriptors Derived from Frontier Orbitals and DFT Computed Electrostatic Potential Energy Surface Maps. *Int. J. Photoenergy* **2016**, *2016*, No. 6765805, DOI: 10.1155/2016/6765805.

(48) Panwar, U.; Singh, S. K. Atom-Based 3D-QSAR, Molecular Docking, DFT, and Simulation Studies of Acylhydrazone, Hydrazine, and Diazene Derivatives as IN-LEDGF/P75 Inhibitors. *Struct. Chem.* **2021**, *32*, 337.

(49) Babas, H.; Khachani, M.; Warad, I.; et al. Sofosbuvir Adsorption onto Activated Carbon Derived from Argan Shell Residue: Optimization, Kinetic, Thermodynamic and Theoretical Approaches. *J. Mol. Liq.* **2022**, *356*, No. 119019.

(50) Dagdag, O.; El Harfi, A.; El Gouri, M.; Safi, Z.; Jalgham, R. T. T.; Wazzan, N.; Verma, C.; Ebenso, E. E.; Pramod Kumar, U. Anticorrosive Properties of Hexa (3-Methoxy Propan-1,2-Diol) Cyclotri-Phosphazene Compound for Carbon Steel in 3% NaCl Medium: Gravimetric, Electrochemical, DFT and Monte Carlo Simulation Studies. *Heliyon* **2019**, *5*, No. e01340, DOI: 10.1016/j.heliyon.2019.e01340.

(51) Erdoğan, Ş.; Safi, Z. S.; Kaya, S.; Işın, D. Ö.; Guo, L.; Kaya, C. A Computational Study on Corrosion Inhibition Performances of Novel Quinoline Derivatives against the Corrosion of Iron. *J. Mol. Struct.* **2017**, *1134*, 751−761, DOI: 10.1016/j.molstruc.2017.01.037.

(52) El Hammari, L.; et al. Optimization of the Adsorption of Lead (II) by Hydroxyapatite Using a Factorial Design: Density Functional Theory and Molecular Dynamics. *Front. Environ. Sci.* **2023**, *11*, No. 1112019.

(53) Ajebli, S.; Kaichouh, G.; Khachani, M.; et al. Modeling of Tenofovir Disoproxil Fumarate Decontamination Using Sodium Alginate-Encapsulated Activated Carbon: Molecular Dynamics, Monte Carlo and Density Functional Theory. *Colloids Surf., A* **2023**, *663*, No. 131057.

(54) Amrhar, O.; Lee, H.-S.; Lgaz, H.; Berisha, A.; Ebenso, E. E.; Cho, Y. Computational Insights into the Adsorption Mechanisms of Anionic

Dyes on the Rutile TiO2 (1 1 0) Surface: Combining SCC-DFT Tight Binding with Quantum Chemical and Molecular Dynamics Simulations. *J. Mol. Liq.* **2023**, *377*, No. 121554.

(55) Fereidoon, A.; Aleaghaee, S.; Taraghi, I. Mechanical Properties of Hybrid Graphene/TiO2 (Rutile) Nanocomposite: A Molecular Dynamics Simulation. *Comput. Mater. Sci.* **2015**, *102*, 220.

(56) Mayo, S. L.; Olafson, B. D.; Goddard, W. A. DREIDING: A Generic Force Field for Molecular Simulations. *J. Phys. Chem.* **1990**, *94*, 8897.

(57) Dagdag, O.; El Gana, L.; Haldhar, R.; Berisha, A.; Kim, S.-C.; Berdimurodov, E.; Hamed, O.; Jodeh, S.; Akpan, E. D.; Ebenso, E. E. Study on Thermal Conductivity and Mechanical Properties of Cyclotriphosphazene Resin-Forced Epoxy Resin Composites. *Crystals* **2023**, *13*, 478.

(58) Ongari, D.; Boyd, P. G.; Kadioglu, O.; MacE, A. K.; Keskin, S.; Smit, B. Evaluating Charge Equilibration Methods to Generate Electrostatic Fields in Nanoporous Materials. *J. Chem. Theory Comput.* **2019**, *15*, 382.

(59) El Gaayda, J.; Ezzahra Titchou, F.; Oukhrib, R.; Karmal, I.; Abou Oualid, H.; Berisha, A.; Zazou, H.; Swanson, C.; Hamdani, M.; Akbour, R. Ait Removal of Cationic Dye from Coloured Water by Adsorption onto Hematite-Humic Acid Composite: Experimental and Theoretical Studies. *Sep. Purif. Technol.* **2022**, *288*, No. 120607.

(60) Hasani, N.; Selimi, T.; Mele, A.; Thaçi, V.; Halili, J.; Berisha, A.; Sadiku, M. Theoretical, Equilibrium, Kinetics and Thermodynamic Investigations of Methylene Blue Adsorption onto Lignite Coal. *Molecules* **2022**, *27*, 1856.

(61) Mehmeti, V.; Halili, J.; Berisha, A. Which Is Better for Lindane Pesticide Adsorption, Graphene or Graphene Oxide? An Experimental and DFT Study. *J. Mol. Liq.* **2022**, *347*, No. 118345.

(62) Iroha, N. B.; Anadebe, V. C.; Maduelosi, N. J.; Nnanna, L. A.; Isaiah, L. C.; Dagdag, O.; Berisha, A.; Ebenso, E. E. Linagliptin Drug Molecule as Corrosion Inhibitor for Mild Steel in 1 M HCl Solution: Electrochemical, SEM/XPS, DFT and MC/MD Simulation Approach. *Colloids Surf., A* **2023**, *660*, No. 130885.

(63) Tang, C.; Farhadian, A.; Berisha, A.; Deyab, M. A.; Chen, J. Supporting Information Novel Biosurfactants for Effective Inhibition of Gas Hydrate Agglomeration and Corrosion in Offshore Oil and Gas. *ACS Sustainable Chem. Eng.* *111* 353 367.   DOI: 10.1021/acssuschemeng.2c05716.

(64) Iravani, D.; Esmaeili, N.; Berisha, A.; Akbarinezhad, E.; Aliabadi, M. H. The Quaternary Ammonium Salts as Corrosion Inhibitors for X65 Carbon Steel under Sour Environment in NACE 1D182 Solution: Experimental and Computational Studies. *Colloids Surf., A* **2023**, *656*, No. 130544.

(65) Lebkiri, I.; Abbou, B.; Hsissou, R.; et al. Investigation of the Anionic Polyacrylamide as a Potential Adsorbent of Crystal Violet Dye from Aqueous Solution: Equilibrium, Kinetic, Thermodynamic, DFT, MC and MD Approaches. *J. Mol. Liq.* **2023**, *372*, No. 121220.

(66) Ajebli, S.; Kaichouh, G.; Khachani, M.; et al. The Adsorption of Tenofovir in Aqueous Solution on Activated Carbon Produced from Maize Cobs: Insights from Experimental, Molecular Dynamics Simulation, and DFT Calculations. *Chem. Phys. Lett.* **2022**, *801*, No. 139676.

(67) El Nemr, A. Eco-Friendly Synthesis and Characterization of Double-Crossed Link 3D Graphene Oxide Functionalized With Chitosan for Adsorption of Sulfamethazine From Aqueous Solution: Experiment and DFT Calculations. *Front. Environ. Sci.* **2022**, *10*, No. 930693, DOI: 10.3389/fenvs.2022.930693.

(68) Rahimi, A.; Farhadian, A.; Berisha, A.; Shaabani, A.; Varfolomeev, M. A.; Mehmeti, V.; Zhong, X.; Yousefzadeh, S.; Djimasbe, R. Novel Sucrose Derivative as a Thermally Stable Inhibitor for Mild Steel Corrosion in 15% HCl Medium: An Experimental and Computational Study. *Chem. Eng. J.* **2022**, *446*, No. 136938.

(69) Berisha, A. Unraveling the Electronic Influence and Nature of Covalent Bonding of Aryl and Alkyl Radicals on the B12N12 Nanocage Cluster. *Sci. Rep.* **2023**, *13* (1), No. 752, DOI: 10.1038/s41598-023-28055-8.

(70) Amrhar, O.; Berisha, A.; El Gana, L.; Nassali, H.; Elyoubi, M. S. Removal of Methylene Blue Dye by Adsorption onto Natural Muscovite Clay: Experimental, Theoretical and Computational Investigation. *Int. J. Environ. Anal. Chem.* **2023**, *103*, 2419.

(71) Ulusoy, S.; Akalin, R. B.; Çevikbaş, H.; Berisha, A.; Oral, A.; Boşgelmez-Tinaz, G. Zeolite 4A as a Jammer of Bacterial Communication in Chromobacterium Violaceum and Pseudomonas Aeruginosa. *Future Microbiol.* **2022**, *17*, 861.

(72) Berisha, A. An Experimental and Theoretical Analysis of Supercritical Carbon Dioxide Extraction of Cu (II) and Pb (II) Ions in the Form of Dithizone Bidentate Complexes. *Turk. J. Chem.* **2022**, *46*, No. 8, DOI: 10.55730/1300-0527.3362.

(73) Berisha, A.; Seydou, M. Grafting of Aryl Radicals onto Surfaces— A DFT Study. In *Aryl Diazonium Salts and Related Compounds. Physical Chemistry in Action*; Springer, Cham, 2022; pp 121−135.

(74) Danisman, M.; Berisha, A.; Dagdag, O.; Oral, A. Surface Modification of Hydroxyapatite with Enzyme-Catalyzed Reaction: Computation-Supported Experimental Studies. *Mater. Chem. Phys.* **2022**, *289*, No. 126448.

(75) Hamed, R.; Jodeh, S.; Hanbali, G.; Safi, Z.; Berisha, A.; Xhaxhiu, K.; Dagdag, O. Eco-Friendly Synthesis and Characterization of Double-Crossed Link 3D Graphene Oxide Functionalized With Chitosan for Adsorption of Sulfamethazine From Aqueous Solution: Experimental and DFT Calculations. *Front. Environ. Sci.* **2022**, *10*, No. 930693.

(76) Tang, C.; Farhadian, A.; Berisha, A.; Deyab, M. A.; Chen, J.; Iravani, D.; Rahimi, A.; Zhang, Z.; Liang, D. Novel Biosurfactants for Effective Inhibition of Gas Hydrate Agglomeration and Corrosion in Offshore Oil and Gas Pipelines, ACS Sustain. *Chem. Eng.* **2023**, *11*, 353.

(77) Ould Abdelwedoud, B.; Damej, M.; Tassaoui, K.; Berisha, A.; Tachallait, H.; Bougrin, K.; Mehmeti, V.; Benmessaoud, M. Inhibition Effect of N-Propargyl Saccharin as Corrosion Inhibitor of C38 Steel in 1 M HCl, Experimental and Theoretical. *Study, J. Mol. Liq.* **2022**, *354*, No. 118784.

(78) Jodeh, S.; Jaber, A.; Hanbali, G.; Massad, Y.; Safi, Z. S.; Radi, S.; Mehmeti, V.; Berisha, A.; Tighadouini, S.; Dagdag, O. Experimental and Theoretical Study for Removal of Trimethoprim from Wastewater Using Organically Modified Silica with Pyrazole-3-Carbaldehyde Bridged to Copper Ions. *BMC Chem.* **2022**, *16* (1), No. 17, DOI: 10.1186/s13065-022-00814-0.

(79) Nairat, N.; Hamed, O.; Berisha, A.; Jodeh, S.; Algarra, M.; Azzaoui, K.; Dagdag, O.; Samhan, S. Cellulose Polymers with β-Amino Ester Pendant Group: Design, Synthesis, Molecular Docking and Application in Adsorption of Toxic Metals from Wastewater. *BMC Chem.* **2022**, *16* (1), No. 43, DOI: 10.1186/s13065-022-00837-7.

(80) Hamed, O.; Berisha, A.; Dagdag, O.; Janem, A.; Azzaoui, K.; Al-Kerm, R.; Al-Kerm, R.; et al. Cellulose Powder Functionalized with Phenyl Biguanide: Synthesis, Cross-Linking, Metal Adsorption, and Molecular Docking. *BioResources* **2021**, *16*, 7263.

(81) Sadiku, M.; Selimi, T.; Berisha, A.; Maloku, A.; Mehmeti, V.; Thaçi, V.; Hasani, N. Removal of Methyl Violet from Aqueous Solution by Adsorption onto Halloysite Nanoclay: Experiment and Theory. *Toxics* **2022**, *10*, 445.

(82) Amrhar, O.; Berisha, A.; El Gana, L.; Nassali, H.; Elyoubi, M. S. Removal of Methylene Blue Dye by Adsorption onto Natural Muscovite Clay: Experimental, Theoretical and Computational Investigation. *Int. J. Environ. Anal. Chem.* **2023**, *103*, 2419−2444, DOI: 10.1080/03067319.2021.1897119.

(83) Khalaf, B.; Hamed, O.; Jodeh, S.; Bol, R.; Hanbali, G.; Safi, Z.; Dagdag, O.; Berisha, A.; Samhan, S. Cellulose-Based Hectocycle Nanopolymers: Synthesis, Molecular Docking and Adsorption of Difenoconazole from Aqueous Medium. *Int. J. Mol. Sci.* **2021**, *22*, No. 6090, DOI: 10.3390/ijms22116090.